The shielding design concept for the ISODAR neutrino target

View the article online for updates and enhancements.

TECHNICAL REPORT

The shielding design concept for the ISODAR neutrino target

Adriana Bungau,[a,1] **Jose Alonso,**[a] **Larry Bartoszek,**[b,c] **Janet M. Conrad,**[a] **Edward Dunton**[b] **and Michael H. Shaevitz**[b]

[a]*Department of Physics, Massachusetts Institute of Technology,*
77 Massachusetts Avenue, Cambridge, MA 02139, U.S.A.

[b]*Department of Physics, Columbia University,*
538 West 120th Street, New York, NY 10027, U.S.A.

[c]*Bartoszek Engineering,*
818 W. Downer Place, Aurora, IL 60506-4904, U.S.A.

E-mail: abungau@mit.edu

ABSTRACT: The IsoDAR sterile-neutrino search requires a very high intensity neutrino source. For IsoDAR, this high intensity is produced using the high neutron flux from a 60 MeV, 10 mA proton beam striking a beryllium target that floods a sleeve of highly-enriched Li-7. Through neutron capture the Li-7 is transmuted to Li-8, which beta-decays giving the desired high neutrino flux for very-short baseline neutrino experiments. The target can be placed very close to can existing large neutrino detector, which is typically located deep underground to reduce backgrounds. With such a setup, it is necessary to design a shielding enclosure for the target to prevent neutrons from causing unacceptable activation of the rock walls close to the target. Various materials have been studied including steel to thermalize the high energy neutrons and two new types of concrete developed by Jefferson Laboratory, one very light with shredded plastic aggregate, and the other one enriched with high quantities of boron. The shielding is asymmetrical, having a larger thickness towards the detector in order to suppress the neutron and gamma background in the neutrino detector. Simulation results for rock activation and for detector backgrounds are presented.

KEYWORDS: Models and simulations; Targets (spallation source targets, radioisotope production, neutrino and muon sources)

---

[1]Corresponding author.

Contents

1 General considerations

The shielding design for high energy facilities and particle accelerators has become a key aspect of radiation protection due to the deep penetration of high energy neutrons. Protection against neutron radiation is obtained by using appropriate thicknesses and proper types of shielding materials that will slow down the high energy neutrons in the first stage and then absorb the slow neutrons in the second stage to reduce the neutron radiation to acceptable levels. The IsoDAR experiment, in combination with KamLAND detector in Japan [1], will perform sensitive short-baseline neutrino oscillation searches and electro-weak measurements associated with beyond-the-standard-model physics. The requirements for shielding and radiation protection, according to Japanese law, must be in conformance with IAEA recommendations [2]. In accordance with these requirements, the rock activation of the cavern wall due to artificially produced radionuclides must not exceed 0.1 Bq/g. The radiation exposure will be maintained as low as reasonably achievable through shielding around the beam-dump neutrino source. The effectiveness of the shielding will be actively monitored by radiation instruments located in the control room and by frequent area-surveys performed by health physics personnel. Additional shielding is also required to reduce the unwanted neutron and gamma interactions in the KamLAND detector that could cause significant backgrounds for the physics measurements.

The current paper aims to present a reliable solution to the target shielding problem based on two criteria: the neutron flux limitation determined experimentally by irradiating the cavern rock samples in the MIT reactor and the activation limits of the cavern walls, set by the Japanese law in conformance with IAEA recommendations. The current design is an improved and more complete version of the shielding presented in the Conceptual Design Report [3]. While this set-up may not be the ultimate shielding design, the proposed design is a feasible solution to both criteria and fulfils the physics requirements regarding the neutrino background in KamLAND as well. A final, optimised design that will include the total cost, including the cost of the shielding (materials, excavation etc.) will be decided at a later stage.

This paper is organised as follows. Section 2 describes the conceptual design of the IsoDAR system as outlined in the Conceptual Design Report [3, 4]. Shielding considerations regarding the neutron flux limitations, rock analysis and shielding material choice and combinations are presented in section 3. The Monte Carlo simulations and validation with experimental data and MCNPX (Monte Carlo N-Particle eXtended) studies follow in section 4. Material performance and design optimization are presented in section 5. The simulation results of rock activation and radionuclides produced are discussed in section 6 while the results for neutron and photon background estimates in KamLAND detector are presented in section 7.

2 The IsoDAR experiment

At present, the particle physics community is placing a high priority on investigating neutrino masses, oscillations, and mixings [5, 6]. Although in the 3-neutrino oscillation model the three mixing angles and masses associated with three standard neutrino flavors are relatively well known, anomalous results have been observed at LSND [7], MiniBooNE [8] and short-baseline reactor experiments [9]. These inconsistencies can be explained with the hypothesis of a (3+N) sterile neutrino model in which there are three light neutrino mass states and N more massive sterile

neutrino states. IsoDAR is a proposed neutrino experiment that is being developed to do a definitive search for sterile neutrinos in the $\sim 1\,\text{eV}^2\ \Delta m^2$ mass region.

The IsoDAR experimental program will produce a high intensity $\bar{\nu}_e$ beam from the β^- decay of ^{8}Li. The $\bar{\nu}_e$ can interact in the detector via the inverse beta decay (IBD) process: $\bar{\nu}_e + p \rightarrow e^+ + n$. In addition, IsoDAR also represents an important technological step, in terms of producing high-power cyclotrons that can be used for a number of physics and non-physics applications [10–12].

2.1 The IsoDAR design

The IsoDAR conceptual design consists of an ion source which injects up to 50 mA of H2+ into a high-power cyclotron that is required to capture and accelerate up to 5 mA of H2+ ions up to 60 MeV/ amu. Immediately after extraction, the molecular H2+ is dissociated into two protons, with 10 mA of protons delivered to the target system. The ^{9}Be target will produce a high neutron flux that will then enter a sleeve surrounding the target, which contains 99.995% pure ^{7}Li (figure 1).
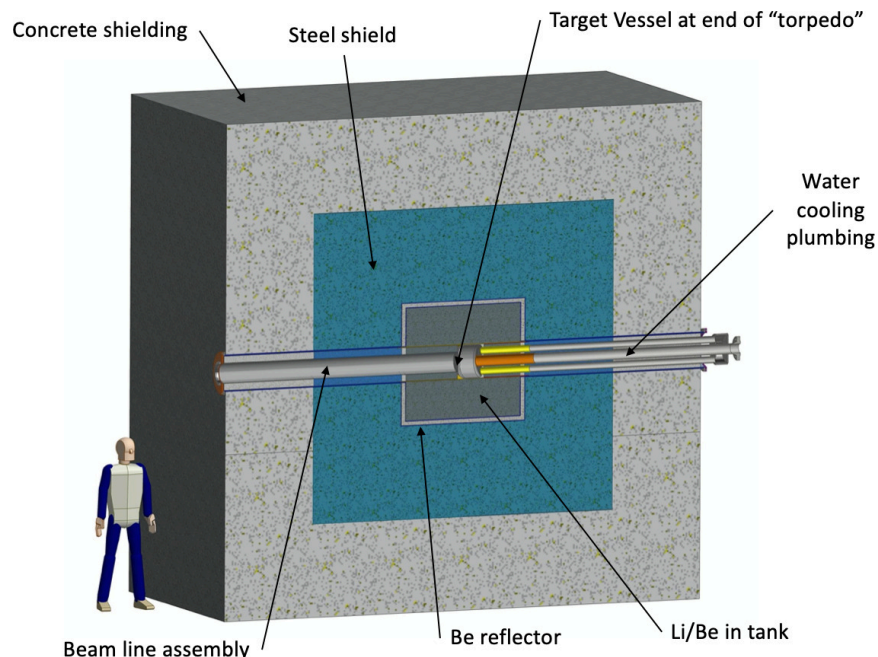

Figure 1. The current layout of the target and shielding system. The target torpedo is surrounded by LiBe sleeve (dark grey) and Be reflector (grey). The target system is enclosed in shielding (steel and concrete mixtures).

The neutron capture on ^{7}Li will create ^{8}Li isotopes which will then beta decay producing the electron antineutrinos. In the conceptual design the sleeve material is a mixture of lithium-floride and beryllium-floride (FLiBe), but recent studies have shown that a homogeneous mixture of lithium and beryllium with an optimum beryllium fraction mass of 75% has a better efficiency of production of ^{8}Li yield [13]. The system is enclosed in a beryllium reflector to enhance the neutron capture on ^{7}Li. When coupled with the KamLAND detector, IsoDAR will observe 8.2×10^5 reconstructed IBD events in five years of 90% duty factor running. With this data set, IsoDAR will provide 5σ

sensitivity to sterile neutrino oscillation models as well as allow precision measurements of $\bar{\nu}_e - e$ scattering and searches for the production and decay of exotic particles [14].

2.2 The IsoDAR shielding

The target assembly is to be placed in the Kamioka mine next to the 1 kton KamLAND liquid scintillator neutrino detector in one of the current utility areas near the detector. The space in this area will have approximate cross section dimensions of 2.25 m floor to ceiling and 3.5 m side to side. The remaining space after placing the target system will be used for shielding. Preliminary calculations indicated that this space will need to be enlarged, particularly in the vertical direction. Minor excavation of the mine is allowed if it can be accomplished without blasting. At the front and back end of the target system, extra shielding material can be added if required.

3 Shielding considerations

In the shielding design two types of radiation need to be considered: neutrons and gamma rays. Most materials can attenuate gamma rays as the thickness is increased with the higher the atomic number and higher density of material giving greater the attenuation. The total neutron flux that is produced in the target system during the experiment depends on the target and sleeve geometries and their materials. A large fraction of these neutrons will be low energy neutrons. Other neutrons reaching the cavern walls could also come from beam loss in the cyclotron and transport line to the target, but this can be minimized by reducing beam losses and providing active monitors that interrupt the beam when abnormally high neutron levels are detected. Additional shielding will be used to reduce the irradiation from the flux produced from unavoidable beam loss.

3.1 Neutron flux limitation

The neutrons that escape the shielding around the target will produce rock activation in the cavern walls. Radionuclides with half-lives shorter than days, or even months, are of no consequence, but the progenitors of long-lived products (i.e. ^{60}Co, ^{152}Eu, ^{154}Eu, ^{134}Cs etc.) need to be assessed. Rock samples were collected from various sites in the mine in close proximity to the experiment location, and were irradiated in the reactor at MIT with a flux of $10^{18}n/cm^2$. An analysis of the irradiated samples was performed at MIT and at LBNL and determined the presence of cobalt and europium at the parts-per-million levels. As progenitors of ^{152}Eu, ^{154}Eu and ^{60}Co these concentrations provide a measure of the upper limit of allowed neutron flux to exit the outer surface of the shielding. From these measurements and calculations, a limit is set at $10^{-13}n/p/mm^2$ neutrons into the cavern walls.

3.2 Shielding materials

The KamLAND detector is a delicate and sensitive large detection instrument and any mining activity in the close proximity of the detector needs to be minimized. Therefore, minimizing the total volume of rock that must be removed for the IsoDAR target cavern is a prime requirement, which can be accomplished with the careful selection of target shielding material. The choice of shielding is strongly dependent on neutron energy, so an efficient combination of materials must shield against the entire range of neutron energies. There are several factors that must be taken

into account when selecting the shielding materials. Considerations such as effectiveness, strength, resistance to damage and cost efficiency can affect radiation protection in many ways. While metals are strong and resistant to radiation damage, they undergo changes in their mechanical properties and degrade in time from radiation exposure. On the other hand, concrete materials are strong, durable and cost effective however they are weaker at elevated temperatures and less effective at blocking neutrons. There is a large range of materials and combinations that can be used and the materials used in this study were selected from a set of compound materials taking into account radiation shielding performance and physical and thermal properties.

First, the fast neutrons must be slowed down via inelastic scattering by using appropriate metal based attenuation materials like iron (carbon steel or stainless steel). Once the neutrons are slowed down to thermal energies by inelastic collisions, then in a second stage the thermal neutrons are captured by the absorbing material. Low-Z materials containing a high fraction of hydrogen (for example water, plastic, concrete) can provide good neutron energy attenuation as a result of elastic scattering of neutrons on protons. At these neutron energies the interaction cross section is high and the energy lost in a collision is significant. However, water is not a reliable candidate as it can evaporate and leak while plastic materials are expensive. Concrete is a good candidate as it is inexpensive and combines many of the good aspects required for shielding, particularly when different materials can be added as aggregates to the mixture. The Jefferson Laboratory (JLab) recently developed new shielding materials, a plastic concrete which performs better than other materials for neutron thermalisation and a boron rich concrete which absorbs neutrons using less material [15].

By adding shredded plastic which contains more hydrogen atoms to the concrete, one can increase its ability to thermalise neutrons while decreasing its weight. Also, by removing the grit and rocks that are normally found in concrete to make it even lighter, the plastic concrete is basically two thirds of the weight of the normal concrete and four times better at thermalising neutrons. The boron rich concrete is basically Portland cement in which the normal rock/sand aggregate is replaced by pelletised boron carbide. In concrete, the neutrons are thermalised when they strike hydrogen atoms in the water molecules that are trapped during the concrete mixing process. Boron has a high neutron capture cross section and has been generally used for neutrino shielding in addition to concrete. The final product is a much better absorber and has the same consistency as ordinary concrete and several layers of boron concrete were used in our studies. Therefore, the current IsoDAR shielding consists of a combination of high-Z and low-Z materials which satisfies the requirements mentioned above.

4 Monte Carlo simulations

4.1 The physics model

There are several Monte Carlo simulation packages used for shielding calculations and, for the calculations of the efficiency and performance of the shielding materials described in this paper, the Geant4 simulation program was used.[1] The Geant4 modelling included the geometrical setup described before and the corresponding material properties, as well as the characteristics of the incoming proton beam.

---

[1]More information on the Geant4 physics models can be found in the Physics Reference Manual: http://geant4-userdoc.web.cern.ch/geant4-userdoc/UsersGuides/PhysicsReferenceManual/html/index.html.

The physics package *particle_hp* used in the current shielding simulations, comprises a set of hadronic models for proton and neutron inelastic interactions for an energy range up to 200 MeV. The package works with Geant4 versions *geant4.9.5* and later and uses evaluated nuclear data bases for inelastic interactions of proton, neutron, deuteron, triton, He3, alpha and gamma. *Particle_hp* includes three physics lists: one for protons *QGSP_BIC_PHP*, one for neutrons *QGSP_BIC_NHP*, and one for all particles, i.e. neutrons, protons, deuterons, tritons, He3, alpha and gamma, *QGSP_BIC_AllHP*. The abbreviation QGSP stands for the Quark Gluon String Parton model, BIC for the Binary Intranuclear Cascade and HP for the high-precision neutron package which includes evaluated neutron data for neutron interactions below 20 MeV. The last two physics lists give the same results for neutrons as the physics list *QGSP_BIC_HP*. The evaluated nuclear data libraries differ and, thus, the results of the Monte Carlo simulations will depend on the library. Two databases *ENDF/B-VII.1* [16] and *TENDL-2014* [17] were used for cross sections of primary and secondary particle interactions. The *ENDF/B-VII.1* library uses experimental data for projectile energies up to 150 MeV, which are essentially nuclear reaction cross sections together with the distribution in energy and angle of the secondary reaction products. Also, it contains data only for 49 isotopes, including Be. The *TENDL-2014* library uses some experimental data and *TALYS* [18] calculations for projectile energies up to 200 MeV. It contains information for all isotopes and can be applied to all target materials but the best results are obtained for targets with atomic number in the range 12–289. For neutron energies below 20 MeV, the high-precision model is employed, which uses *ENDF/B-VII.1*, JENDL [19], MENDL-2 [20] and other data libraries [21]. The Binary Intranuclear Cascade model is called for neutron energies above 20 MeV. This model includes a low energy nuclear de-excitation model called the G4Precompound model which is called by the simulation when the particle energy is below 100 MeV and when the nuclear structure effects start to play an important role.

4.2 Validation studies

Differential neutron yields for several angles and various beam energies were measured in References [22]–[28]. New measurements of the neutron yield produced by a 62 MeV proton beam on a thick beryllium target were performed at Laboratori Nazionali del Sud (LNS) of INFN using the existing superconducting cyclotron [29]. A 62 MeV proton beam with an operating beam current of 30–50 pA was extracted from the cyclotron and transported through the beam transport system to the target. The beryllium target had a thickness of 3 cm and 3.5 cm diameter. This thickness was chosen to ensure complete absorption of the protons. The neutrons produced in the target were measured by the time-of-flight technique. Eight neutron detectors were installed around the target, at the same height with respect to the beamline, with different angles and with two different distances (150 cm and 75 cm). The electric charge deposited by the beam on the target was measured by a digital current integrator and used for absolute normalization of the data.

The target and the detector set up were modelled in the Geant4 simulations. The *particle_hp* physics package was used to simulate the neutron yield produced by 62 MeV protons and figure 2 shows the results at 0°, 30°, 90° and 150°. The comparison of the simulation with the experimental data taken from ref. [29] and also from refs. [22, 23], and [24] at 0° for lower beam energies shows a significant disagreement in the lower neutron energy range. This disagreement demonstrates lower beam energy data cannot be extrapolated to higher beam energies simply by an overall factor since
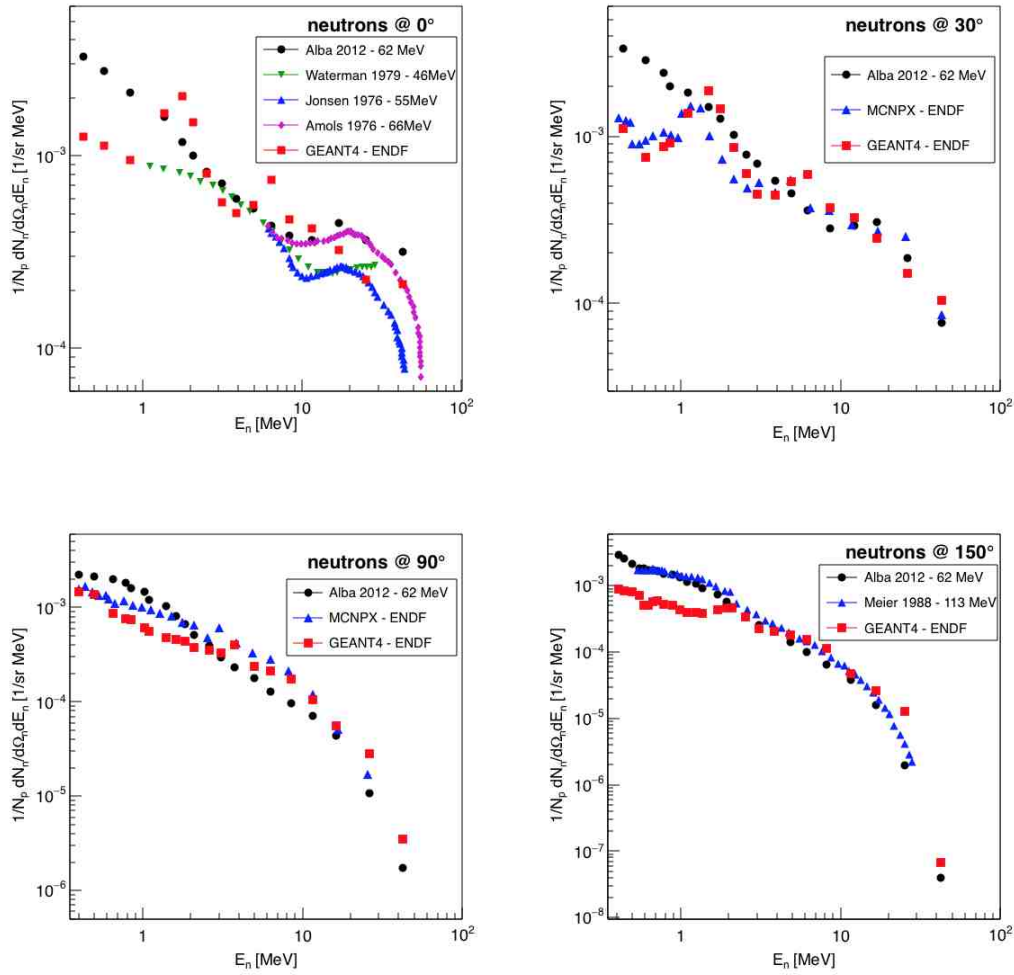
Figure 2. Comparison of the *particle_hp* physics package predictions with the experimental data taken from ref. [29] , ref. [2–5] and MCNPX simulations. The neutron yield was measured at 0°, 30°, 90° and 150°. The proton energy is 62 MeV in all the Geant4 simulations.

the kinematic limits have to be taken into account. For low energy neutrons (below 10 MeV) there is a disagreement between data and simulation especially at lower angles. The *ENDF VII* database library for particle cross sections was released in December 2011 and therefore it does not contain the experimental results measured in ref. [29] at the later date. However, at larger angles, there is a good agreement between these two, even for low energy neutrons (above 2 MeV). At larger angles (150°) there is a good agreement between the measured data in ref. [29] and ref. [25] with the Geant4 code predictions for neutron energies above 2 MeV. At neutron energies below 1–2 MeV, the Geant4 predictions lie below the data. However these low energy neutrons will not make it through the shielding and therefore will not pose a problem for the rock activation studies.

The Geant4 simulations were then compared with MCNPX results [31] using the ENDF data library for the measured cross sections. The comparison shows good agreement between the predictions of the two codes at larger angles, 30° and 90°. There is a good agreement between the two codes and the data in some kinematic regions at larger angles and larger neutron energies.

The experimental measurements in ref. [29] which are not included in the ENDF/B-VII proton database, show a difference about a factor of two greater than the values obtained with the two simulation packages below 1–2 MeV. However simulation values are higher in the range 2–70 MeV, so overall we expect the experimental and simulated neutron yields values integrated over the entire energy range (1–70 MeV), to be similar. This has been shown to be indeed the case in the validation study [13] performed against the experimental measurements of neutron fluxes published in ref. [30].

As more experimental data for protons on beryllium become available, they will be added to the proton ENDF database increasing the accuracy of the model predictions. The current predictions of the *particle_hp* model rely on the existing tabulated experimental data and will improve as the new data is implemented. The validation studies presented above as well as previous studies of 60 MeV protons on beryllium [13] have shown that the *particle_hp* model with the ENDF data library describes the proton inelastic interactions on Be for 60 MeV incident energy better than any other theoretical model available, justifying its selection for these studies.

5   Shielding design

5.1   Material performance

Simulations were carried out to asses the performance of the selected shielding materials. Neutron shielding materials with variable thickness placed in different arrangements were examined and the comparisons are shown in this section. As the area where the target system and the surrounding shielding will be located was once a construction tunnel for KamLAND, its dimensions are not overly generous. The cross section of the cavern which measures roughly 2.3 m high by 3.5 m wide leaves ≈50 cm from the target system to the ceiling. As the available vertical space is the critical dimension in our Monte Carlo modelling, the figure of merit in the simulations is the neutron flux recorded on the ceiling, at 90 degrees with respect to the beam direction. Initial studies using inner layers of plastic concrete for neutron moderation and outer layers of boron rich concrete for neutron absorption for the available ~50 cm showed that the neutron flux was several orders of magnitude higher than the desired value of $10^{-13}n/p/mm^2$. These results implied that rock will need to be removed to place an adequately shielded target in this tunnel. A summary of all the materials combinations, total shielding thickness and the neutron flux obtained in the simulations is shown in table 1.

Assuming that a minimum of 50 cm of rock will be removed from the cavern ceiling, a target shielding of total thickness of maximum 100 cm of various combinations of plastic concrete and boron rich concrete was considered. The thickness of each material layer was 10 cm in our simulations. The neutron flux recorded at 90 degrees on a detector sphere was still above the desired value, $10^{-13}n/p/mm^2$ (figure 3). This was due to the fact that the fast neutrons would escape the 100 cm of shielding, suggesting thus that more high-Z material is required to attenuate them. The inelastic scattering on high-Z atoms reduces the neutron energy to a much lower value and they are absorbed in the boron rich concrete layers. Therefore, in addition to the 100 cm shielding of plastic

Table 1. The material combinations and the total shielding thickness used in the simulations.

Materials Combinations	Total thickness	Neutron flux
plastic concrete and boron loaded concrete	100 cm	above $\Phi = 10^{-13}n/p/mm^2$
20 cm steel, plastic concrete and boron loaded concrete	120 cm	some below $\Phi = 10^{-13}n/p/mm^2$
steel and boron loaded concrete	120 cm	some below $\Phi = 10^{-13}n/p/mm^2$
steel and boron loaded concrete	200 cm	below $\Phi = 10^{-13}n/p/mm^2$

concrete and boron rich concrete, two layers of 20 cm total thickness of steel were added. In this configuration, the inner layers are steel, followed by variable thicknesses of plastic concrete. The outer layers are boron rich concrete to absorb the neutrons. The results are shown in figure 4.
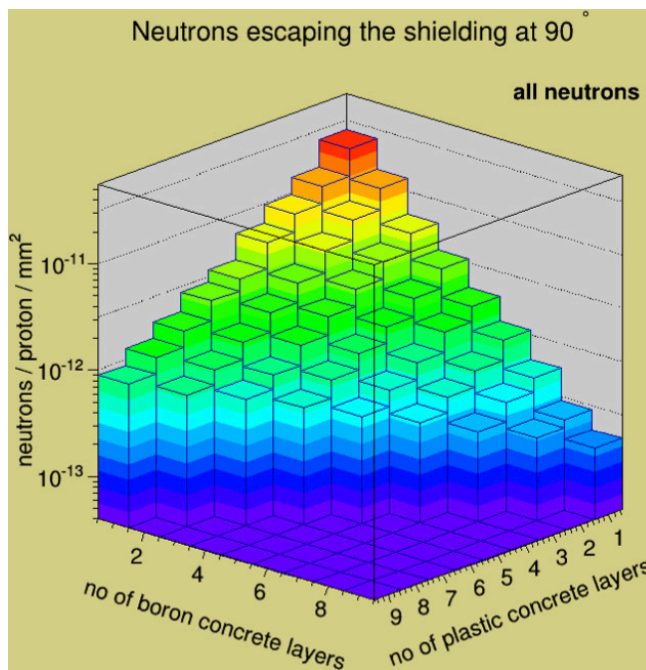

Figure 3. The neutron flux escaping the shielding at a 90 degrees angle with respect to the proton beam direction. The shielding consists of combinations of layers of plastic concrete and boron rich concrete, each layer being 10 cm thick. The total shielding thickness is up to 100 cm. The neutron flux is above the desired value $10^{-13}n/p/mm^2$ for all combinations. (The purple combinations are not considered since they have total thicknesses greater than 100 cm.)

There are several material combinations for which the neutron flux is lower than $10^{-13}n/p/mm^2$ (left plot). The flux is lowest for the combination 20 cm steel, 10 cm plastic concrete and 90 cm boron rich concrete. As figure 4 suggests, the optimum solution is for a minimum thickness of plastic concrete and indicates that better results can be obtained for combinations of steel and boron rich
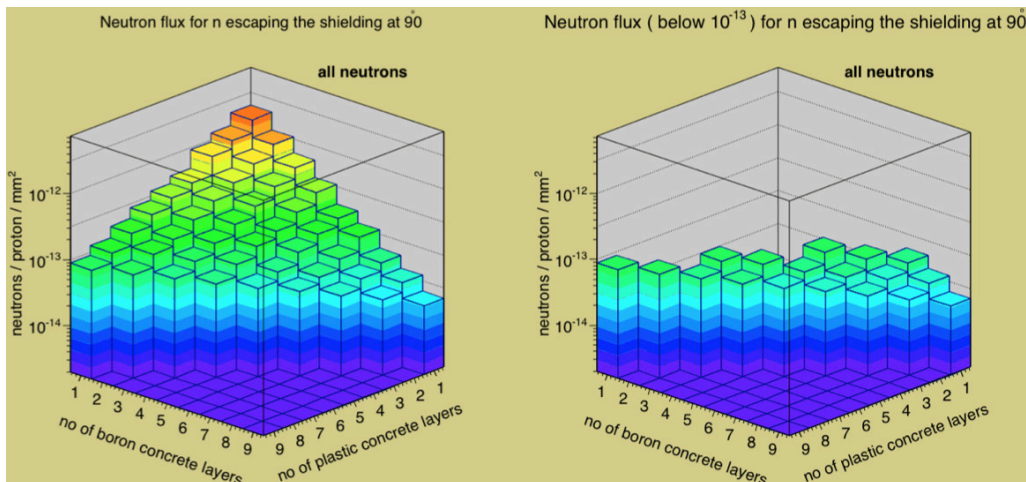
Figure 4. The neutron flux out of the shielding at 90 degrees with respect to the beam direction. The shielding consists of two inner layers of steel of 20 cm total thickness (not shown), followed by combinations of layers of plastic concrete and boron rich concrete (left plot). Each layer has 10 cm thickness and the total shielding thickness is up to 120 cm. The right plot shows only those combinations for which the neutron flux is below the desired value $10^{-13} n/p/mm^2$.
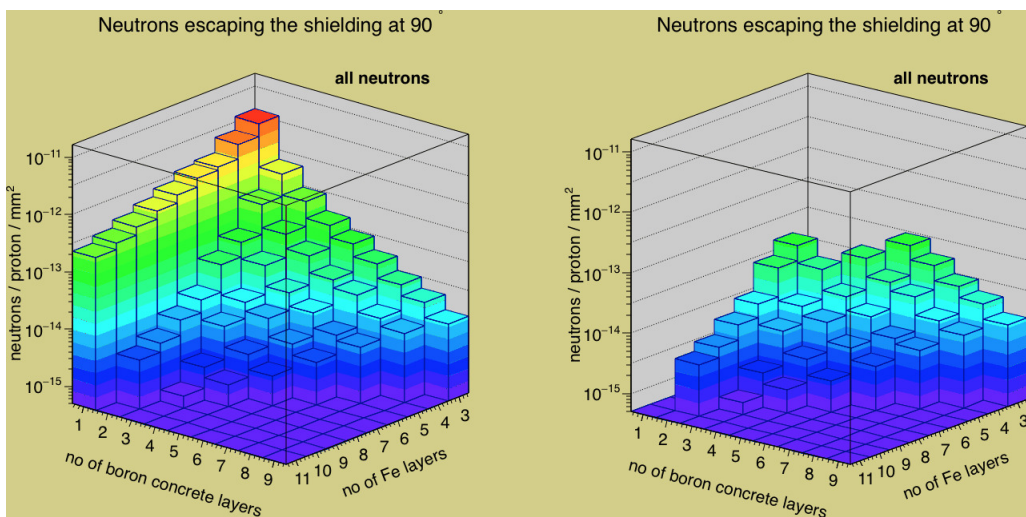

Figure 5. The neutron flux escaping the shielding at 90 degrees with respect to the beam direction, using only combinations of layers of steel and boron concrete, but no plastic concrete. Each layer is 10 cm thick and the total thickness is up to 120 cm (left plot). For some combinations, the flux is much lower in this case than when plastic concrete was present and lower than the desired value $10^{-13} n/p/mm^2$ (right plot).

concrete only. The same total shielding thickness of 120 cm was maintained but plastic concrete was removed completely. The results are shown in figure 5. The neutron flux can be brought down to $10^{-15} n/p/mm^2$ for 90 cm of steel and 30 cm of boron concrete. However, the baseline configuration of 30 cm steel and 90 cm boron concrete was chosen for the rock activation analysis

as it contains a minimum number of steel layers, so overall a lower shielding mass (165,331 kg).

The neutron flux for this particular shielding configuration (30 cm steel and 90 cm boron rich concrete) was recorded on a detector sphere of radius 3.5 m and the results are shown in figure 6. The beam travels from right to left in figure 6. The lower flux values at 40 and 140 degrees correspond to the corners of the concrete shielding block and the higher values of flux above 140 degrees correspond to neutrons escaping into the space left for the wobbler magnets in front of the target where additional shielding can be placed. Of greatest interest in this study is the flux at 90 degrees, or neutrons penetrating through the thinnest point of the bulk shielding. The average neutron flux at 90 degrees for all energies is $1.88 \times 10^{-15} n/p/mm^2$. It should be noted from figure 6 that there is an appreciable number of neutrons at 0 and 180 degrees that escape the shielding block. The very high 'wings' at low and high angles point to holes in the shielding for beam entry and target servicing. As seen below, addition of more shielding both upstream and downstream can adequately control these higher fluxes. As distance along the axis of the beam does not impact cavern size, such additions have little consequence on the rock excavation question.
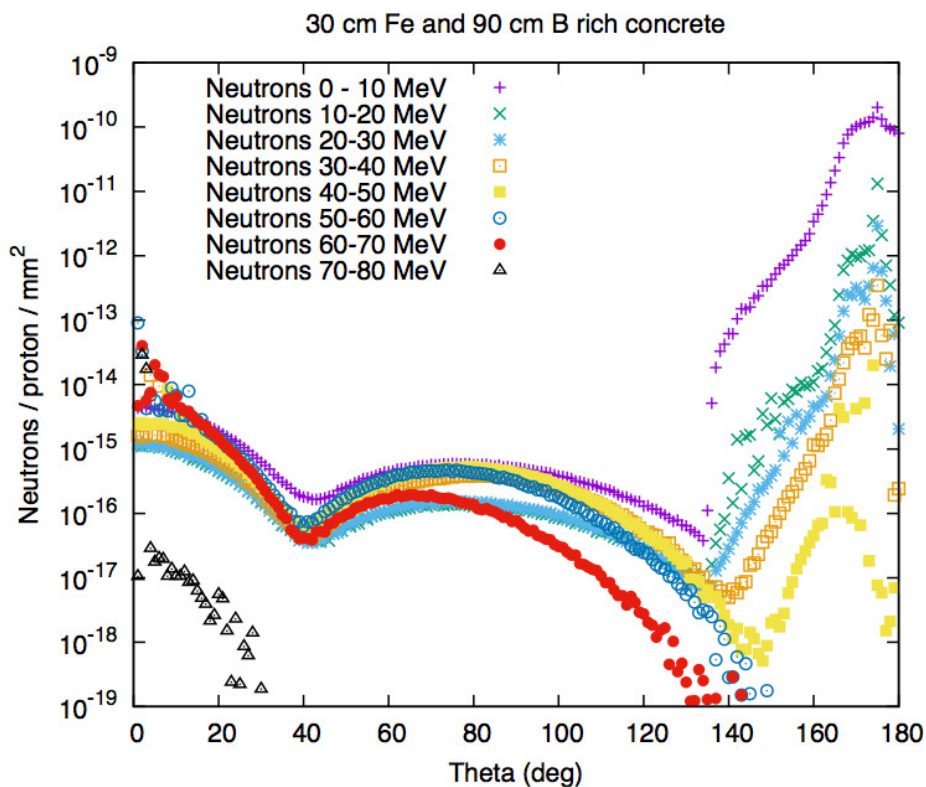

Figure 6. The neutron flux detected on a sphere surrounding the shielding. The sphere radius is 350 cm. The shielding material consists of 30 cm Fe and 90 cm boron rich concrete. The high values of neutron flux at 0 and 180 degrees correspond to holes in the shielding for beam entry and target servicing.

To obtain a more accurate calculation of the neutron flux, simulated detector plates were placed on the shielding block to record the flux at 0, 90 and 180 degrees for this baseline shielding configuration with 30 cm of steel and 90 cm of boron rich concrete. The neutron flux detected at the front and at the back of the shielding block is shown in figure 7. The neutron contamination in the proton beam pipe has a peak value of $2.4 \times 10^{-6} n/p/mm^2$ while the flux in the space left for the wobbler magnets has a peak value of $1.4 \times 10^{-6} n/p/mm^2$.
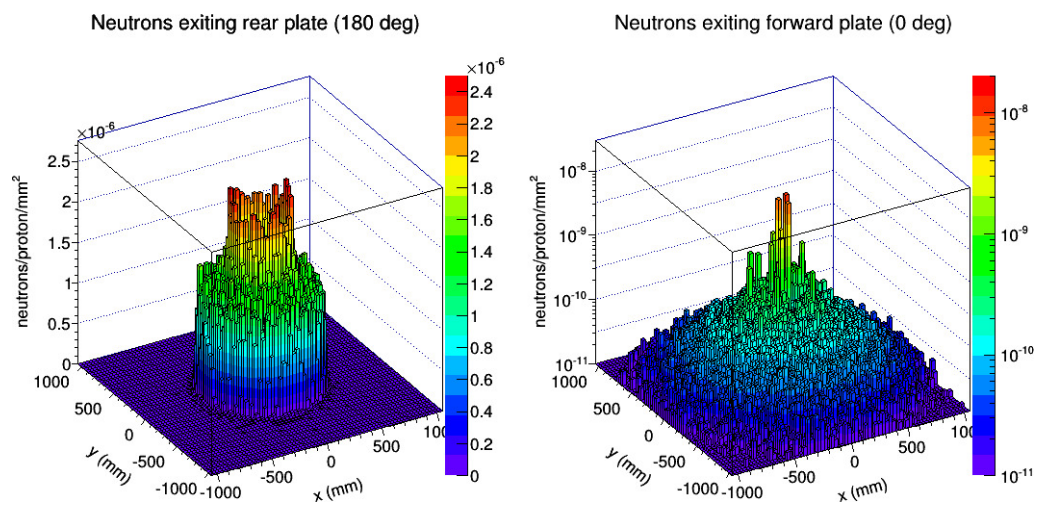

Figure 7. Neutron flux recorded on detector plates placed at 0 and 180 deg on the target shielding. The shielding is made of 30 cm steel and 90 cm boron rich concrete.
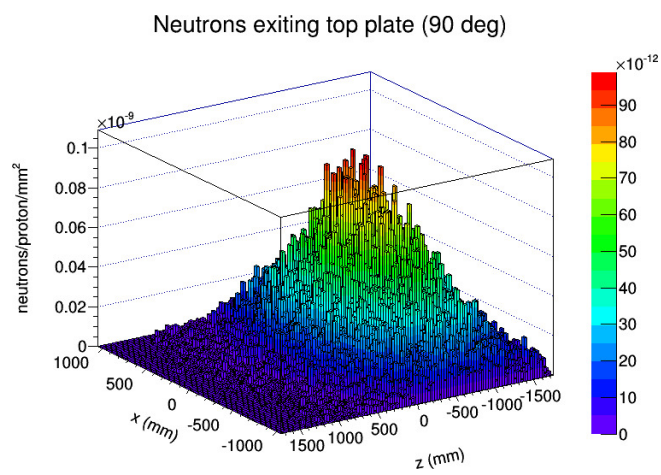

Figure 8. Neutron flux at 90 deg for a shielding consisting of 30 cm steel and 90 cm boron rich concrete. The neutron levels can be translated into rock activation, as shown in the next section.

The neutron flux detected on the plate above the shielding block (figure 8) is forward biased, as most of the neutrons that are backscattered escape in the space left for the magnets and therefore have no chance to be scattered into the sleeve and detected on the first half of the plate. The average neutron flux is $4 \times 10^{-11} n/p/mm^2$.

5.2 Design optimisation

Slight changes to this design were imposed by the fact that a large fraction of backscattered neutrons escape in the space left for the wobbler magnets without being moderated and captured by shielding. To avoid this, the hole at the front end of the target system was sealed with shielding, leaving space only for the proton beam pipe. The wobbler magnet will be placed outside the shielding block, as well as the 30 degree bending magnet. This new configuration will adequately block the escaping neutron flux in the upstream direction (figure 9). The forward neutron flux (at low angles) can be further attenuated by using movable blocks of steel and concrete. There is much less of a space restriction at the beam height, so added material can be readily provided. This extra material needs to be movable to enable changing of the target assemblies, which occurs from the downstream side of the target complex.
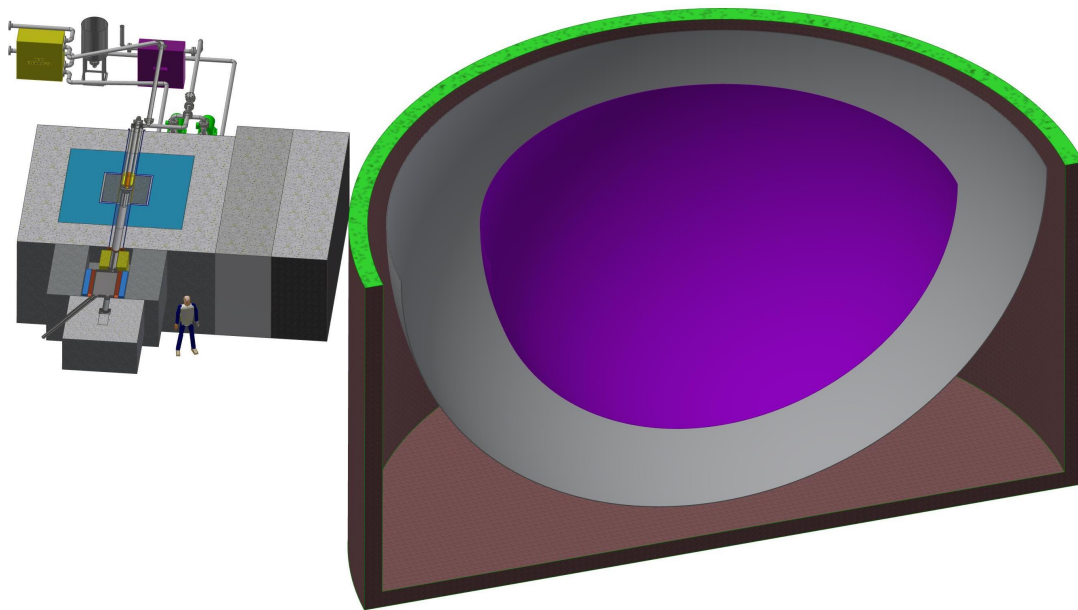

Figure 9. Aerial view of the target and shielding system, with the wobbler magnet and bending magnet placed outside the shielding block. The water cooling system is placed at the back of the target. The KamLAND detector with the surrounding buffer region and water layer is also shown.

Figure 10 shows that the neutron flux after improvements to the target shielding. The holes at the front and at the back of the target were filled with shielding material. The material combination was changed to 40 cm steel and 80 cm boron rich concrete for better neutron attenuation. The neutron flux is much lower in this design as seen in figure 10. The detector sphere radius is 7 m as it surrounds not just the target system but also the wobbler magnet and the neutron trap.

6 Rock activation studies

Although the parametric studies of neutron flux versus shielding composition suggested a preliminary design for which the neutron flux was below the desired value, the ultimate shielding
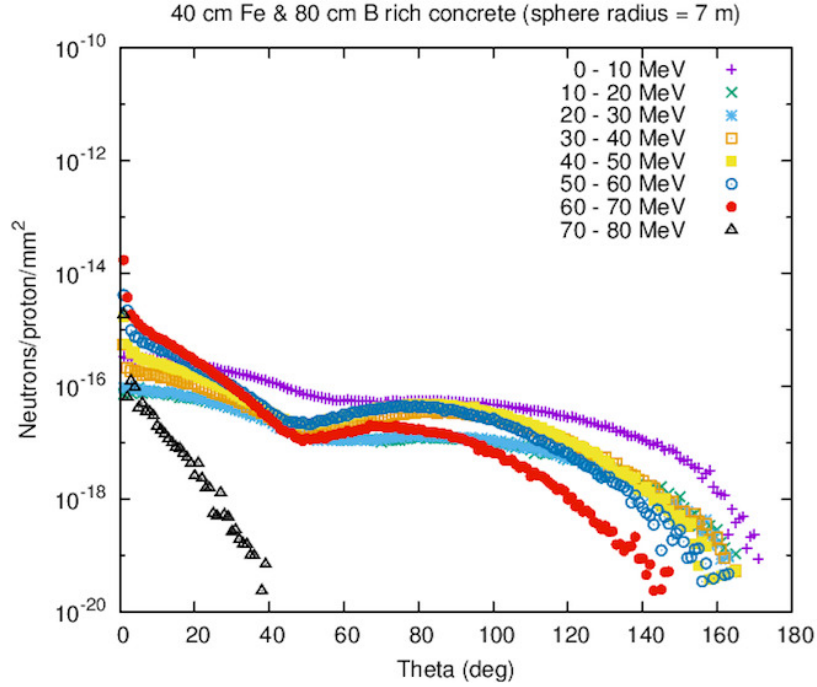
Figure 10. The neutron flux detected on a sphere surrounding the shielding after seal in the space for magnets. The shielding material consists of 40 cm steel and 80 cm boron rich concrete.

effectiveness is given by the rock activation of cavern wall which must not exceed 0.1 Bq/g. Therefore, the calculation of induced activation and the analysis of the radionuclides produced serve as the guide in designing the final shielding configuration.

6.1 Methodology for calculation of induced activity

The time dependence of the number of radioisotopes produced is given by the individual production and decay rate of each isotope. The production rate for a radioactive isotope is given by:

$$\frac{dN_i^{\text{prod}}}{dt} = \frac{N_{\text{iso}}}{\Delta t} = \frac{N_{\text{iso}}I}{N_p e} \tag{6.1}$$

where N_{iso} is the number of isotopes produced by the simulation, I is the current, N_p is the number of simulated protons, and e is the proton charge. Once the radioisotopes are produced, they decay exponentially with time. The decay rate for each isotope i is a function of its decay constant:

$$\frac{dN_i^{\text{decay}}(t)}{dt} = -\lambda_i N_i(t) \tag{6.2}$$

During the beam-on period, the time evolution can be obtained by combining the production and decay rates:

$$\frac{dN_i(t)}{dt} = \frac{N_{\text{iso}}I}{N_p e} - \lambda_i N_i(t) \tag{6.3}$$

The solution of eq. (6.3), gives the number of isotopes at any time t during the beam exposure:

$$N_i(t) = \frac{N_{\text{iso}}I}{N_p e \lambda_i}(1 - \exp(-\lambda_i t)) \tag{6.4}$$

However, after the beam is switched off, following a continuous exposure for a time t_1, the number of isotopes after a time t, which includes both the beam on period t_1 as well as a beam off period t_2, is given by:

$$N_i(t) = \frac{N_{\text{iso}}I}{N_p e \lambda_i}(1 - \exp(-\lambda_i t_1)) \exp(-\lambda_i(t_2)) \tag{6.5}$$

The induced activity given by one particular isotope is given by eq. (6.6):

$$A_i(t) = \lambda_i N_i(t) \tag{6.6}$$

Using eq. (6.5) and eq. (6.6), the activity of each isotope produced can be given at any given time t which includes the beam on time t_1 and the beam off time t_2. The total induced activity given by all isotopes is given by eq. (6.7):

$$A(t) = \sum_i \lambda_i N_i(t) \tag{6.7}$$

The production rates of all isotopes produced in the rock are required further for calculation of the total induced activity.

6.2 KamLAND rock composition

KamLAND is located under the peak of Ikenoyama (Ike Mountain, 36.42°N, 137.31°E). Various types of rocks are found in Ikenoyama in unknown quantities, such as Inishi type rocks, skarn rocks, but also granite and limestone. The Inishi type rock is characteristic for the Japanese mountains and is made of various oxides with a high concentration of SiO_2. Skarns are calcium-bearing silicate rocks that are most often formed at the contact zone between intrusions of granitic magma bodies and carbonate sedimentary rocks such as limestone and dolostone. The skarn-type rock is defined as a combination of 70% granite and 30% limestone. The specific gravity for generic skarn is 2.75% g/cm^3 and for the Inishi rock is 2.65 % g/cm^3 [32]. The exact composition of the Inishi rock is given in table 2, [33, 34].

Because some of the longer-lived activation products come from trace concentrations of elements such as Co, Eu, and Cs, rock samples were taken and were analyzed at the MIT reactor by thermal neutron activation (TNA). Figure 11 shows the location where samples were taken from, extending over about a 50 meter distance along one of the access drifts leading to KamLAND.

At the time, this drift was considered the prime site for deployment of IsoDAR. The TNA study identified about 40 different elements, table 3 indicates the concentration of the progenitors of the principal contributors to long-lived activities in the cavern rock determined from the samples from the six sites shown. There are substantial variations in the amount of each element in the TNA analysis, justifying the analysis of multiple samples. In addition, for the Geant4 activation calculations, some amounts were slightly increased (Na from 4% to 5%, and Co from 16 ppm to 30 ppm).

Table 2. Chemical composition of the Inishi-type rock in elemental percentage.

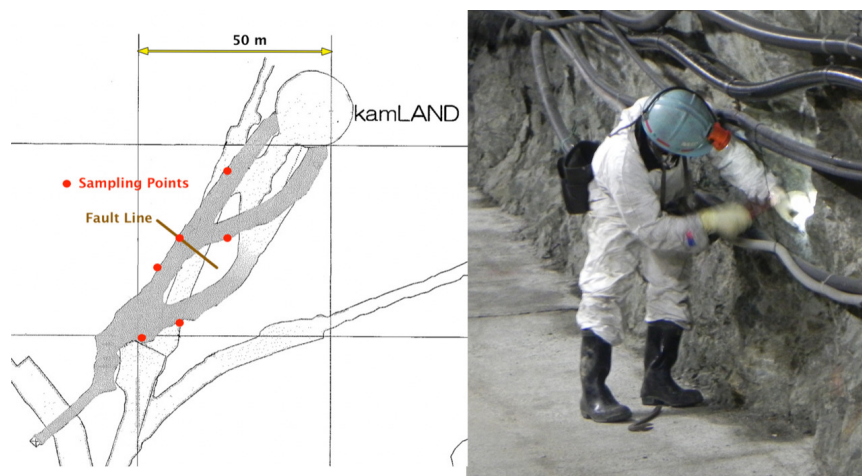| Compound	Composition (%)	Compound	Composition (%)
SiO_2	60.70	CaO	6.00
TiO_2	0.31	Na_2O	6.42
Al_2O_3	17.39	K_2O	3.47
Fe_2O_3	1.10	P_2O_5	0.18
FeO	1.22	H_2O	1.27
MnO	0.15	S	0.01
MgO	0.93	CO_2	0.96

Figure 11. Rock sample collection in the vicinity of KamLAND, at the approximate locations of the accelerator, transport and target station envisioned at the time. Rock was collected by the Kamioka mining employee from six spots along the drift ribs (walls). A clearly visible fault line transected the drift, one sample was collected from the debris along the fault inclusion.

6.3   List of radionuclides produced

The rock compositions given in table 2 and table 3 were used as inputs for Geant4 calculations to establish the production of radioactive isotopes. The geometry assumed was the previously-mentioned shielding thickness configuration of 40 cm steel and 80 cm of boron concrete. The volume of rock evaluated for radioactive isotope production covered the full 4×4 meters of the top surface of the shielding, to a depth of 1 meter into the rock. Isotopes identified by Geant4 were ^{7}Be, ^{22}Na, ^{44}Ti, ^{46}Sc, ^{51}Cr, ^{54}Mn, ^{59}Fe, ^{56}Co, ^{57}Co, ^{58}Co, ^{60}Co, ^{134}Cs, ^{152}Eu and ^{154}Eu. The bar charts in figure 12 show the resulting production rates for each of these isotopes. These bars are the rates of production for each isotope, per incident beam proton. To evaluate the relative importance of each of these isotopes in the ultimate activation of the rock, equation eq. (6.5) was used to include the relevant times and decay rates for each isotope. Short half lives will diminish the importance of a given isotope, as they will decay more rapidly.

Table 3. Elemental composition of Kamioka rock samples determined by Thermal Neutron Activation analysis.

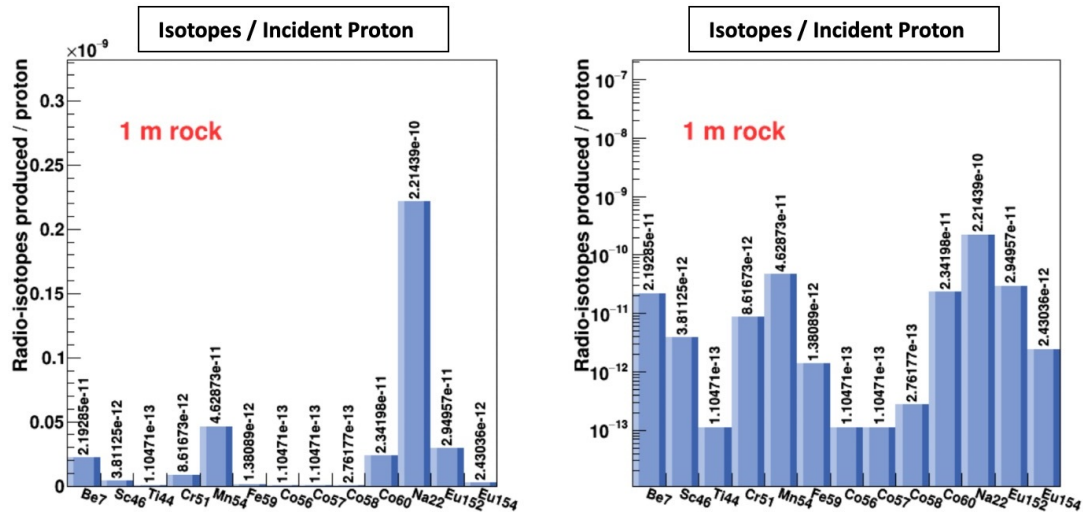| Element	Cobalt	Cesium	Europium	Iron	Sodium
Progenitor for:	^{60}Co	^{134}Cs	^{152}Eu, ^{154}Eu	^{54}Mn	^{22}Na
Rock samples	(ppm)	(ppm)	(ppm)	(%)	(%)
1	5.2	1.5	1.0	1.5	6.5
2	14.1	0.4	3.1	4.3	8.6
3	35.0	5.1	1.0	9.2	3.4
4	0.4	0.0	0.2	0.1	0.0
5	3.9	0.2	0.9	1.9	0.1
6	40.0	9.3	1.1	6.1	1.4
Average	16	3	1	4	3
Std. Dev.	17	4	1	3	4

Figure 12. Rate of the isotope production in 1 m depth of Inishi-type rock. The production rate is dominated by the long-lived isotopes. The shielding consists of 40 cm steel and 80 cm boron concrete.

Table 4 summarizes the most important contributors to residual radioactivity, under the following conditions: total irradiation time — 5 years; beam current — 9 mA (10 mA design current at 90% efficiency); cooling time after end of irradiation — 2 years. ^{22}Na dominates the residual activity levels, followed by ^{54}Mn, ^{60}Co, ^{152}Eu, ^{134}Cs and ^{154}Eu. Contribution from other isotopes is insignificant compared to these. The Bq rates listed in the last column of table 4 represent the total activity in the 16 cubic meter block of rock, but should not be used to evaluate compliance with the 0.1 Bq/gm requirement. The analysis in section 6.4 provides the detailed distribution of these isotopes, and identifies the hottest spots, which should be used for establishing compliance.

Table 4. Characteristics of the isotopes of interest. We assume 5 years of running at 9 mA (1.70E+24 protons). For ^{134}Cs, MIT activation analysis indicated 3ppm Cs, equivalent to 10% of ^{60}Co.

Isotope	Half life	Production rate (Figure 11.)	Total produced	Amount at beam off (Eq. (6.4))	Bq at beam off	Amount after 2yrs cool off	Bq after 2yrs
^{7}Be	53 d	2.20E-11	3.75E+13	1.57E+12	2.38E+05	1.12E+08	17
^{22}Na	2.6y	2.21E-10	3.76E+14	2.08E+14	1.76E+06	1.22E+14	1031144
^{44}Ti	60 y	1.10E-13	1.87E+11	1.82E+11	6.67E+01	1.78E+11	65
^{46}Sc	84 d	3.80E-12	6.47E+12	4.30E+11	4.10E+04	1.04E+09	99
^{51}Cr	27 d	8.60E-12	1.46E+13	1.16E+10	9.29E+04	2.67E-210	0
^{54}Mn	312 d	4.60E-11	7.83E+13	1.90E+13	4.88E+05	3.75E+12	96470
^{59}Fe	44 d	1.40E-12	2.38E+12	8.29E+10	1.51E+04	8.42E+05	0
^{56}Co	77 d	1.10E-13	1.87E+11	1.14E+10	1.19E+03	1.60E+07	2
^{57}Co	271 d	1.10E-13	1.87E+11	3.98E+10	1.18E+03	6.15E+09	182
^{58}Co	71 d	2.80E-13	4.77E+11	2.68E+10	3.02E+03	2.15E+07	2
^{60}Co	5.2 y	2.34E-11	3.98E+13	2.91E+13	1.23E+05	2.23E+13	94166
^{134}Cs	2.06 y	2.30E-12	3.92E+12	1.90E+12	2.02E+04	9.67E+11	10318
^{152}Eu	13.5 y	2.95E-11	5.02E+13	4.43E+13	7.21E+04	4.00E+13	65086
^{154}Eu	8.6 y	2.43E-12	4.14E+12	3.41E+12	8.70E+03	2.90E+12	7408

6.4 Spatial distribution of activity induced at various depths

A rock sample having the same area as the top part of the shielding block and a thickness of 100 cm, was considered in our simulations. The rock sample was placed on top of the shielding block in the Monte Carlo modelling. The rock composition is the same as in table 2 with Co and Eu fractions by weight added. Using the equations above, one can calculate the spatial distribution of induced activity of all isotopes produced at various depths. The rock sample was sliced into 20 layers, each having 5 cm thickness. The total activity is calculated over the entire rock volume, however the highest activity concentration was measured using the central hot spot in the rock sample where the distribution is approximately uniform. Visual inspection of the square in figures 13 and 14 (x and z scales are slightly different, the central square is 100×100) gives the appearance of spatial uniformity, a detailed analysis was not carried out.

But to an arbitrary precision of, say, 25% uniformity is a reasonable assumption. Table 5 also shows that the layer closest to the shielding surface is about 15% hotter than the next layer, so to within the same accuracy 5 cm depth is a justified thickness to assume. The activity in this volume (100×100×5)cm then could be used as the data set to compare to the 0.1 Bq/g requirement. Because of the relatively high variation in the uniformity in this volume, a large margin of safety should be planned. The overall activity in the rock is above the required level of 0.1 Bq/g, and much higher on the central hotspots. As most of the isotopes are short lived, the contribution to the total activity after seven years must be associated with the long lived isotopes like ^{60}Co, ^{152}Eu, ^{154}Eu and ^{22}Na. The
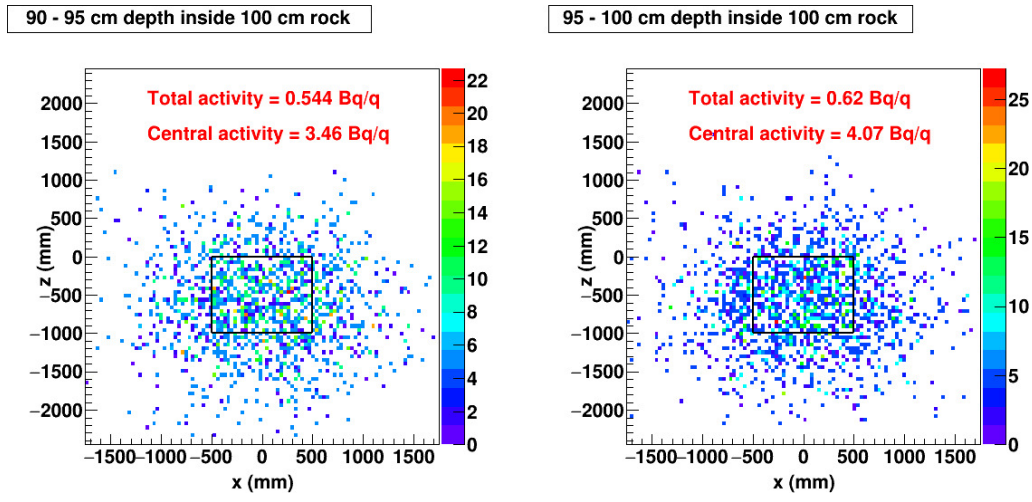
Figure 13. Spatial distribution of induced activity in the lowest layers of the considered rock sample, in the close proximity of the target and shielding system (90–100 cm). The overall activity in the layers is above the required limit of 0.1 Bq/g and much higher in the central hotspots. This analysis is for the 40 cm steel and 80 cm boron concrete shielding.

contributions of these isotopes to the total activity in Bq/g in the central hotspots is shown in table 5 for all 20 rock layers. The ^{22}Na gives the highest activation and it is produced by the fast neutrons escaping from the shielding, indicating that thicker layers of steel are needed for extra safety.

Table 5. Contribution to the total induced activity of isotopes in the central hot spots (100×100 cm) in Bq/g, given by the long-lived isotopes of interest.

Rock layer (cm)	^{60}Co	^{152}Eu	^{154}Eu	^{22}Na	Total	Rock layer (cm)	^{60}Co	^{152}Eu	^{154}Eu	^{22}Na	Total
0–5	0	0	0	0.014	0.053	50–55	0.155	0.048	0	0.354	0.500
5–10	0	0.011	0	0.034	0.052	55–60	0.115	0.064	0.005	0.423	0.823
10–15	0.006	0.011	0	0.061	0.069	60–65	0.126	0.101	0.016	0.682	0.935
15–20	0.017	0.021	0	0.007	0.125	65–70	0.143	0.069	0	0.791	0.986
20–25	0.040	0.005	0	0.061	0.109	70–75	0.138	0.080	0	1.070	1.370
25–30	0.040	0.021	0.005	0.109	0.151	75–80	0.092	0.080	0.011	1.360	1.620
30–35	0.063	0.021	0	0.143	0.208	80–85	0.109	0.112	0.005	1.830	2.040
35–40	0.046	0.043	0	0.232	0.238	85–90	0.149	0.085	0	1.960	2.580
40–45	0.069	0.048	0.005	0.348	0.356	90–95	0.080	0.053	0.011	2.840	3.460
45–50	0.063	0.043	0.005	0.286	0.437	95–100	0.063	0.016	0.005	3.550	4.070

Since for the 120 cm of shielding the induced rock activation exceeds the 0.1 Bq/g limit, despite the neutron flux entering the surrounding rock being below the established threshold, the shilding thickness was increased to 160 cm (100 cm steel and 60 cm B-rich concrete). In order to study the induced activation in the surrounding rock, a much larger number of events was simulated, in order to
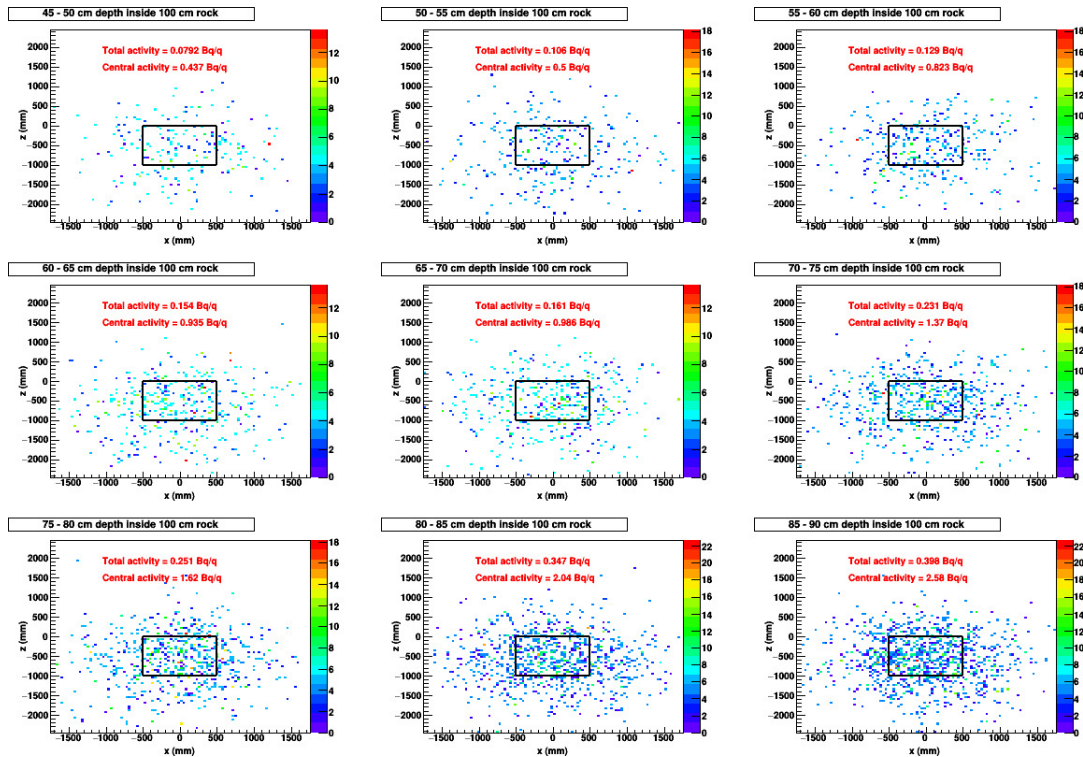
Figure 14. Spatial distribution of induced activity in the upper layers of the considered rock sample (45–90 cm) for the 40 cm steel and 80 cm boron concrete shielding.The overall activity in the layers is above the required limit of 0.1 Bq/g.

improve the overall statistics. The induced activation levels in the rock layers which are closer to the shielding are shown in figure 15, and these results show that the induced activation has a peak value of exactly 0.1 Bq/g. However these results are based on Monte Carlo simulations relying on physics models which, despite the fact that they make use of all the available neutron cross-section libraries, are inevitably based on various assumptions and approximations. For this reason, this study was focused next on additional shielding consisting of 100 cm of steel, and 100 cm of B-rich concrete.

As rock activation studies ultimately evaluate the effectiveness of the shielding, a 2 m shielding consisting of 1 m of steel and 1 m of boron concrete was considered for calculations of the induced activation in the rock layers. The neutron spectra out of the reflector and out of the 2 m shielding is shown in figure 16. This plot also shows the neutron spectra out of the 4 m shielding side towards the KamLAND detector that will be placed between the target and the detector to suppress the neutron and gamma background (figure 9). The 2 m shielding decreases the neutron rates from 2.65×10^{-2} neutrons/POT (out of the reflector) to 6.86×10^{-10} neutrons/POT. With this extra shielding, the activation levels on central spots in the rock layers will also decrease significantly as figure 17 shows for the first 10 cm of rock situated in the proximity of the shielding. The total activity and the activity on the central hotspots for each layer of rock sample was calculated for the 200 cm shielding and the results are shown in table 6.
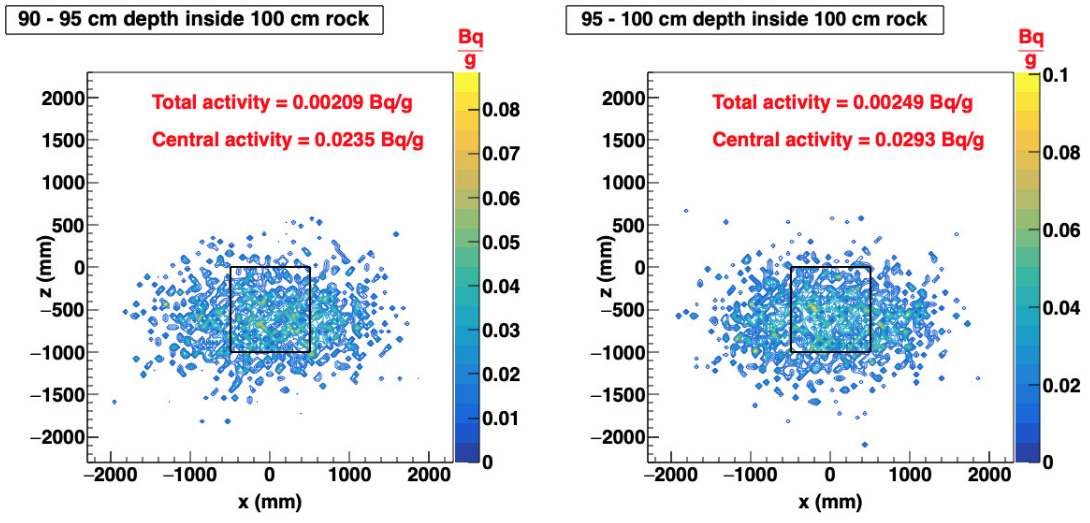
Figure 15. Spatial distribution of induced activity in the lowest layers of the considered rock sample for the 160 cm shielding, in the close proximity of the target and shielding system (90–100 cm). The overall activity in the layers is slightly below the limit of 0.1 Bq/g for most of the region, although there are isolated spots where the activity is exactly at this limit.
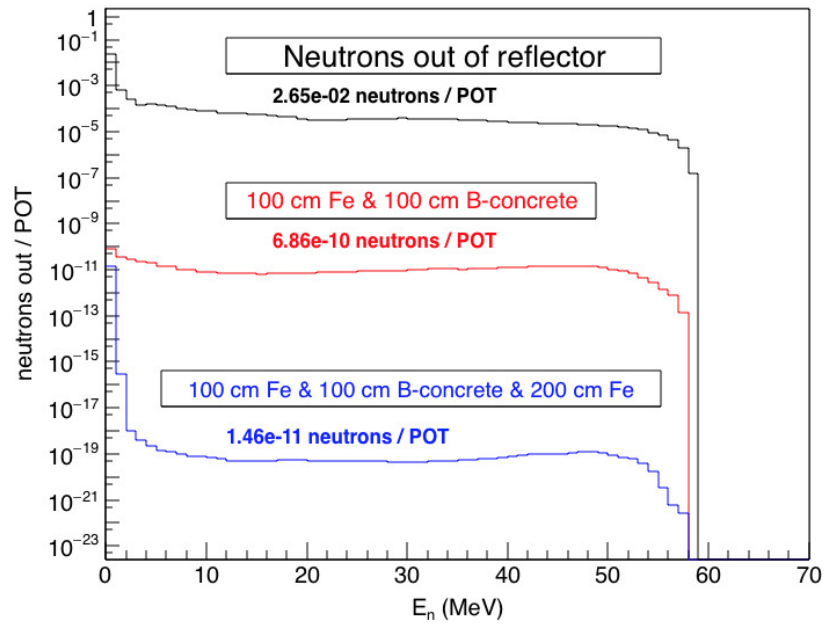

Figure 16. The neutron spectra out of the reflector and out of the 2 m shielding. It also shows the neutron spectra for the 4 m shielding side that fills the available space between the target system and the KamLAND detector (figure 9).
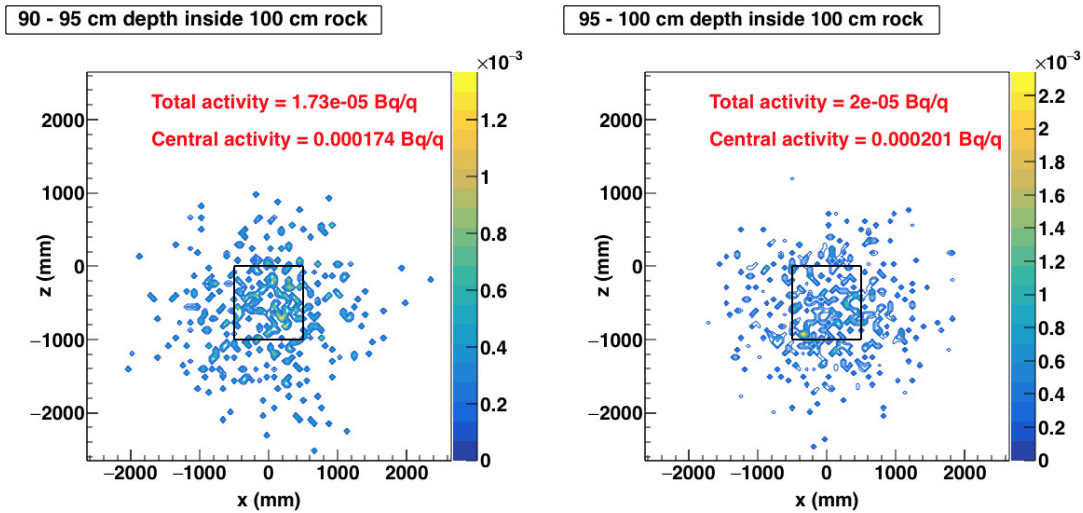
Figure 17. Spatial distribution of induced activity in the lowest layers of the considered rock sample, in the close proximity of the target and shielding system (90–100 cm). The overall activity in the layers is below the required limit of 0.1 Bq/g even in the central hotspots. This analysis is for the 200 cm shielding.

Table 6. The total and central activity on hotspots in each layer of the rock.

Rock layer (cm)	Total activity: $10^{-6}(Bq/g)$	Central activity: $10^{-5}(Bq/g)$	Rock layer (cm)	Total activity: $10^{-6}(Bq/g)$	Central activity: $10^{-5}(Bq/g)$
0–5	0.116	0.113	**50–55**	3.25	2.97
5–10	0.407	0.113	**55–60**	3.89	3.36
10–15	0.663	0.175	**60–65**	5.01	4.3
15–20	0.856	0.917	**65–70**	5.87	4.53
20–25	0.84	1.04	**70–75**	8.28	6.54
25–30	0.859	0.661	**75–80**	8.94	9.4
30–35	1.10	1.07	**80–85**	12.5	10.9
35–40	1.48	1.02	**85–90**	13.4	10.5
40–45	2.4	1.42	**90–95**	17.3	17.4
45–50	2.5	2.53	**95–100**	20	20.1

These numbers are sufficiently below the 0.1 Bq/g that any possible variation in intensity over the sample volume of (100×100×5) cm becomes insignificant. Therefore, 200 cm of total shielding can be considered a safe thickness for compliance with the required activation standard.

6.5 Activity induced in the rock

The total activity in the entire rock sample considered after 5 years run and 2 years beam cool down period is shown in figure 18 with the peak value representing the activity at the beam switch off

time. It can be seen that, for the 200 cm of shielding materials, the induced activity inside the rock is well below the imposed limit of 0.1 Bq/g, both throughout the beam on period, as well as after the beam switch off.
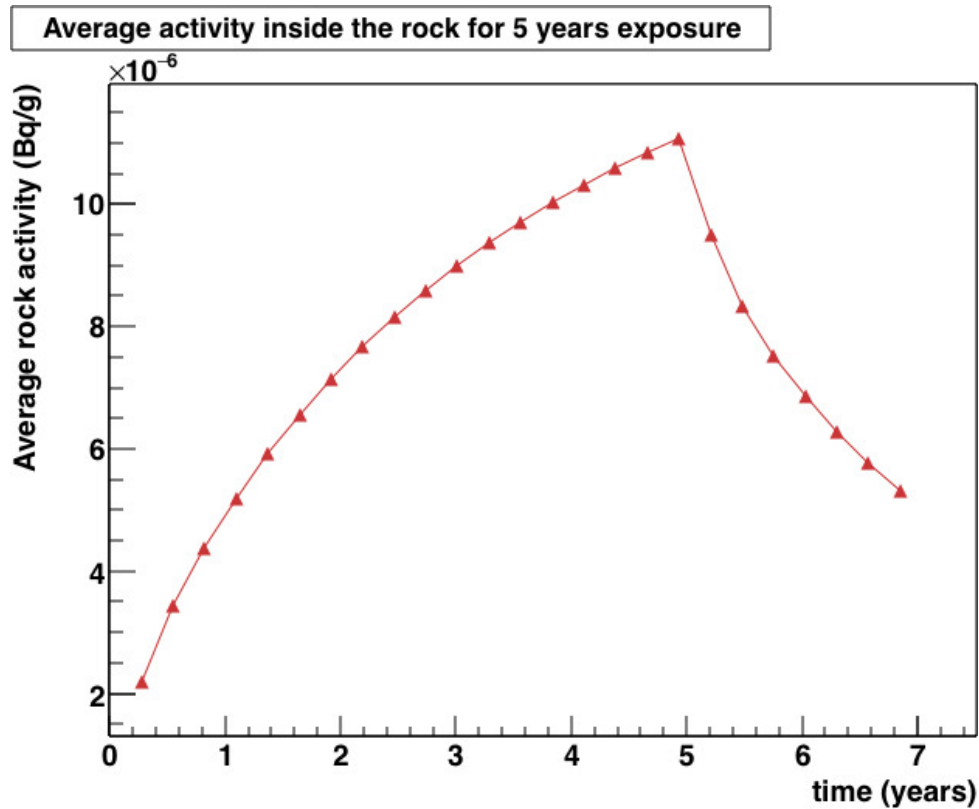

Figure 18. The total averaged activity in the entire rock during beam On and beam Off time. The total shielding thickness is 200 cm.

6.6 Distribution of isotope production with rock height

At the rock surface the slow neutrons will be responsible for surface activation, but faster neutrons will also produce activation at higher levels inside the rock. The isotope production inside the rock varies with the distance from the top layer of shielding. A large fraction of isotopes are produced in close proximity of target-shielding system with the production decreasing with the rock height and reaching a minimal value after 1 m of rock. The ^{22}Na production as a function of rock height is shown in figure 19. As ^{22}Na is a significant component of the rock chemical composition, even a small flux of high energy neutrons can contribute to an unacceptable high ^{22}Na production.

7 Shielding requirements for reducing the neutron and photon physics backgrounds in the KamLAND detector

While the majority of non-beam backgrounds for IsoDAR at KamLAND can be experimentally measured and subtracted by comparing beam-on versus beam-off measurement periods, there are a
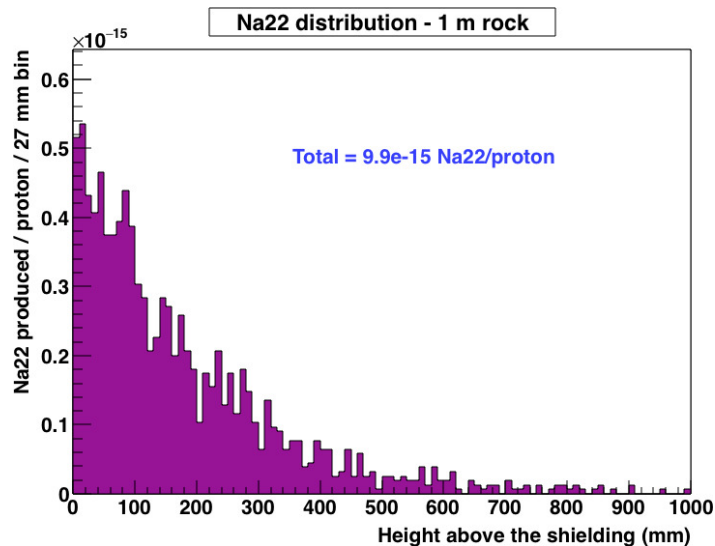
Figure 19. ^{22}Na production as a function of rock height for the 200 cm shielding (100 cm steel and 100 cm boron concrete).

few backgrounds inherent to the beam and target itself that must be accounted for. Most significant of these are neutrons produced by the interaction of the proton beam on the Li-Be target. Many of these neutrons will be captured on the ^{7}Li, which will then decay to produce the electron antineutrinos that are to be measured in the experiment, but there is a significant portion that will not. Geant4 simulations find that approximately 2.65×10^{-2} neutrons per proton-on-target (POT) will escape the neutrino-producing reflector and enter the target shielding. Due to the calculated 7.88×10^{24} POT over IsoDAR's five year run, this represents an unacceptably high background of neutrons into the KamLAND detector that the needs to be reduced through shielding.

IsoDAR will study two kinds of neutrino events during its run. The first are inverse beta decay (IBD) events, of which there will be 8.2×10^5 events over the five year run. These events are characterized by a prompt positron signal with $E_{vis} = E_{\bar{\nu}_e} - 0.78$ MeV coincident with a delayed neutron capture releasing a 2.2 MeV gamma within 200 μs. These events will not be affected by the neutron background since the signal is a two-part delayed coincidence. The second kind of event to be studied is the sample of low-energy $\bar{\nu}_e$-electron scatters (ES). There will be approximately 2600 of these events above a 3 MeV threshold over the five year run, and they will be easily mimicked by elastic scatters of neutrons in the KamLAND detector. Thus, additional shielding is needed to reduce the rate of neutrons and gammas over 3 MeV in the KamLAND detector region to a rate less than about 200 over the five year run.

7.1 Neutron shielding

7.1.1 Target shielding

The IsoDAR target is already shielded by 200 cm of material intended to absorb neutrons in order to comply with Japan's radiation requirements for the surrounding cavern. A full Geant4 simulation from the incoming POT to the neutrons escaping from this shielding showed a final output of just

6.86×10^{-10} neutrons per POT, which drops to 5.40×10^{-10} above the 3 MeV threshold. The majority of these neutrons are oriented away from the KamLAND detector due to the geometry of the target shielding, with many escaping through the vacuum of the beam pipe or the less heavily shielded water access tubes. Additional shielding is placed outside the target cube to further shield these accesses in the interests of radiation reduction, and also helpfully prevents the majority of these neutrons from moving towards the detector.

After the target shielding and accounting for the limited solid angle intercepted by the KamLAND detector, the incoming neutron flux towards the KamLAND detector is reduced to 1.069×10^{-9} neutrons above 3 MeV per POT. This estimate is made after a full simulation starting from incoming beam protons at 60 MeV through the entire target geometry, and then counting the neutrons whose direction of motion will intercept the detector itself, with the assumption that neutrons will scatter as much out of the intercepting solid angle as into it. This assumption allows us to use straight line trajectories for neutrons leaving the target region for the purposes of estimating neutron flux in the detector.

7.1.2 Additional shielding design

The additional shielding will be placed between the IsoDAR target and the KamLAND detector complex, and will be composed of stacked blocks of steel to produce a solid rectangle 2 m thick, 5 m high, and 5 m wide. This shielding block will be slightly off center from the target, with center around 50 cm downstream from the center of IsoDAR. This is because simulations of the full IsoDAR target from POT to escaping neutrons show that the majority of high energy neutrons, that the shielding block is meant to moderate, escape on the downstream end of the target (See figure 20).
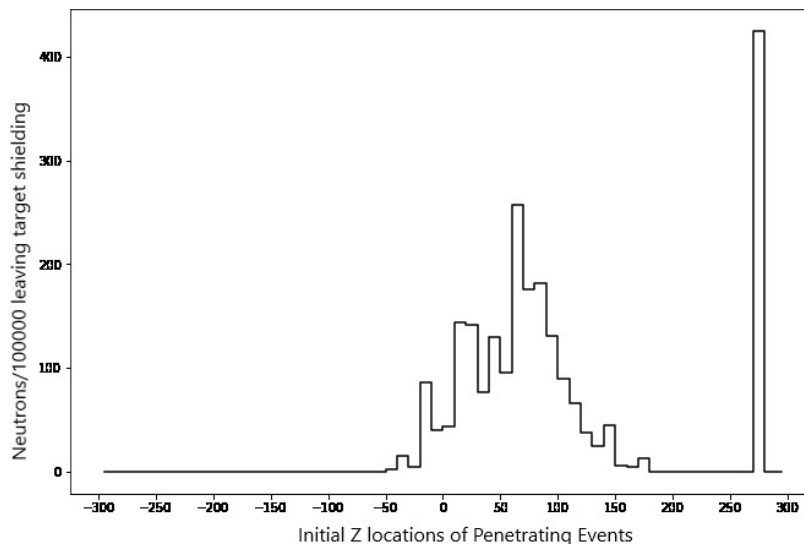

Figure 20. The initial z (along the beam direction with positive downstream) locations of a sample of the neutron events which successfully passed through the KamLAND shielding during the first round of simulation (without the additional 2m of iron). The large spike on the far right represents the excess of neutrons escaping the shielding through the water cooling pipes, which shall be countered by a downstream shift of the additional shielding.

This is due to the water cooling pipes on that end, which provide neutrons an easier path out of the shielding. Unlike the beam pipe on the upstream end, which provides a similar function, these pipes are not encased in additional shielding blocks, so a shift of the additional shielding will be necessary to prevent an excess of neutrons from that end. Fortunately, there is a demonstrated lack of penetrating events from the upstream end which enables this shift without increasing the neutron background by any significant amount.

7.1.3 KamLAND buffer region and additional shielding

Further simulations were based on the neutron energy and direction spectra out of the target shielding and focused on the effectiveness of the KamLAND buffer region in reducing the incoming neutron flux. Unfortunately, while the KamLAND buffer region, at minimum 100 cm of water and 250 cm of paraffin oil, is very effective at capturing and moderating lower energy neutrons less than 10 MeV, it is comparatively far less effective on higher energy neutrons greater than 30 MeV. Incoming neutrons with energy greater than 50 MeV would enter the detector with energy above the threshold of 3 MeV at rates above 1×10^{-3} per neutron, i.e. for every neutron above 50 MeV entering the KamLAND buffer region there will be at least 1×10^{-3} neutrons above 3 MeV entering the detector. This resulted in background rates several orders of magnitude above that desired, with a total above 3 MeV of 5.92×10^{-17} neutrons per POT. Given the 7.88×10^{24} POT over the 5 year run this yields a total background of 4.66×10^{8} neutrons.

These studies demonstrated the need for additional shielding to be added in the 2 m space between the edge of KamLAND and the outer layer of the target shielding. Further, they allowed the prioritization of moderating or slowing high energy neutrons rather than all neutrons in this shielding, as seen in figure 21. As different materials have different moderating effects on different energies of neutrons, this was very useful. Iron was selected as the material of choice in this shielding layer due to its high effective cross section for neutrons between 20 and 60 MeV, the energy domain for penetrating neutrons.
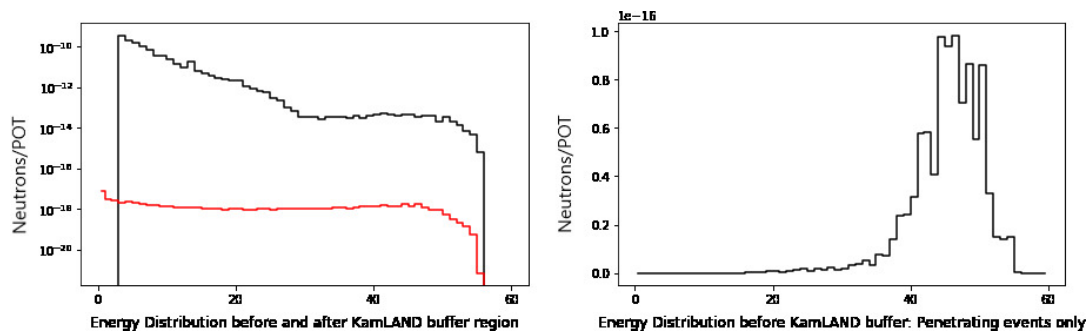

Figure 21. The above left shows the neutron energy distributions (in MeV) before (black) and after (red) the KamLAND buffer region without any additional shielding. The right plot shows the energy distribution of the penetrating neutrons only, i.e. the neutrons that reach the detector with energy > 3 MeV.

As demonstrated in figure 22, the addition of 2m of iron shielding (bringing the total to 4 m) between the end of the target shielding and the start of the KamLAND buffer region drops the penetrating neutrons by nearly 8 orders of magnitude, especially in the higher energy domains where
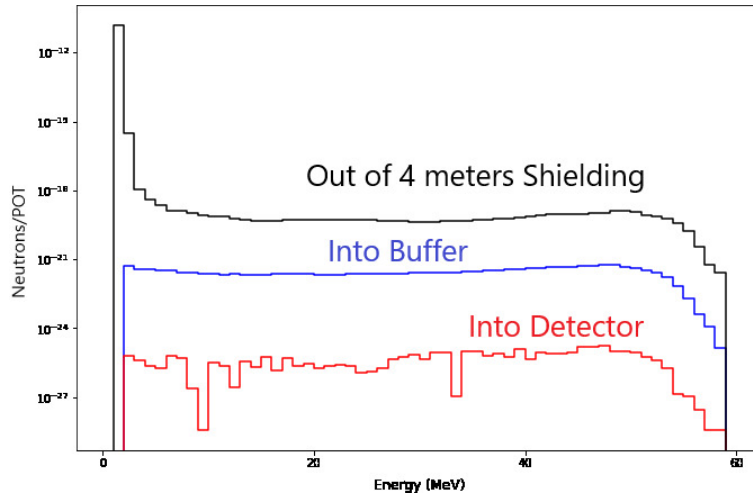
Figure 22. The displayed neutron energy distributions are taken from the simulation of the full geometry of the KamLAND detector and buffer. The simulation started with the neutron energy distribution out of the target and additional 2 m shielding (giving 4m total shielding) (black) and ended with the neutron energy distribution entering into the detector (red), with an intermediate energy check at the transition between the water and mineral oil buffer layers (blue).
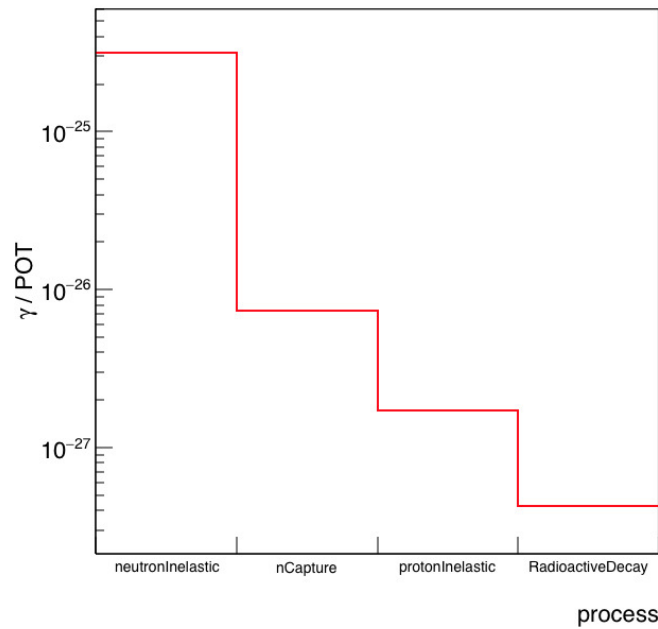

Figure 23. The gammas with energies above 3 MeV that enter the Kamland detector are produced in the buffer regions mainly by neutron inelastic processes. Other processes like neutron capture, proton inelastic and radioactive decay have a lower contribution.
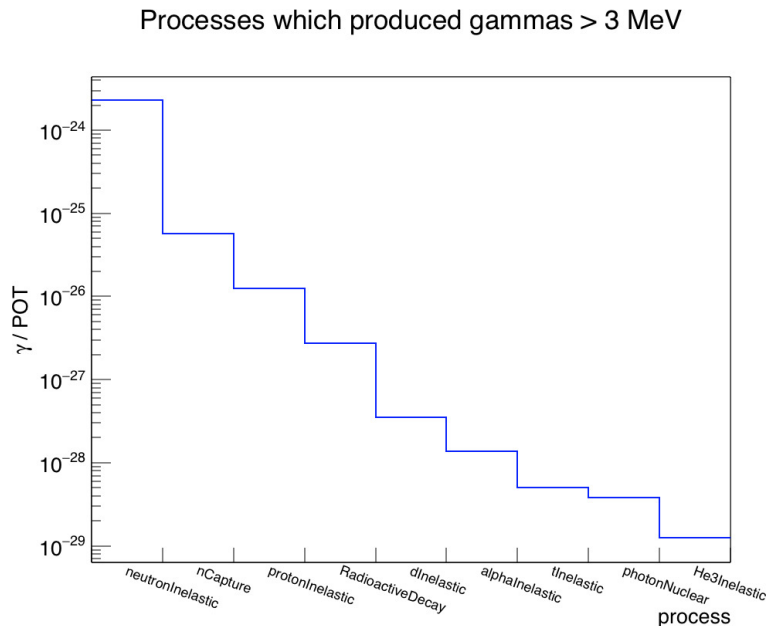
Processes which produced gammas > 3 MeV

Figure 24. Rate of processes that produce gammas with energies above 3 MeV for various particle interactions inside the Kamland detector. Apart from neutron inelastic, neutron capture, proton inelastic and radioactive decay, other processes that give a measurable contribution are deuteron, alpha, triton and He3 inelastic processes, and photon nuclear processes.

the buffer region proved insufficient. All combined, this total shielding left an estimated 2.78×10^{-24} neutrons per POT above the 3 MeV threshold in the KamLAND detector region, which is sufficient to meet our requirements. This represents a mere 22 neutrons above 3 MeV in KamLAND over the entire 5 year run.

This estimate is further taken to be conservative due to the overestimation inherent in the two part simulation, which was made with a rounded up energy distribution to start the second part. IsoDAR will also benefit from beam timing checks that can be used to reduce slow neutron plus energy analyses of the final events. The final neutron distribution in the detector region is essentially homogenous from 3 to 55 MeV, while the ES signal events peak around 10 MeV and do not exceed 20 MeV, as this is the maximum neutrino energy from the ^8Li decays.

7.2 Photon background

The same steel shielding also suppresses the gamma background towards KamLAND. As stated before, the shielding was designed asymmetrically, having a larger thickness towards the detector (4 m) with the extra 2 m filling the space between target and detector. For detector background studies only the neutrons having an energy above 3 MeV are of concern since ES signal to be detected is above 3 MeV. The total number of gammas with energies above 3 MeV that enter the KamLAND detector in a solid angle of 0.17π is 3.26×10^{-25} gammas/POT. These gammas are produced mainly by neutron inelastic processes (3.17×10^{-25} gammas/POT) but at smaller rates also by neutron capture (7.36×10^{-27} gammas/POT). (Figure 23). Photon inelastic processes and
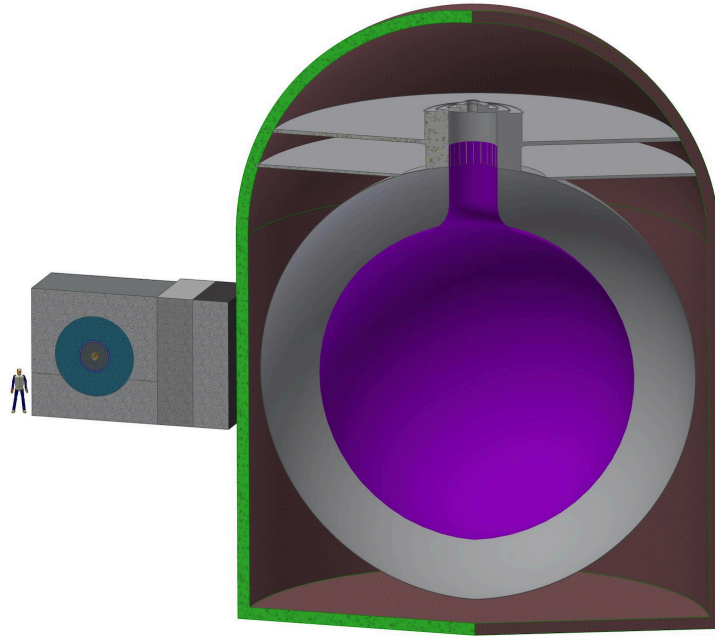
Figure 25. Vertical section through the target shielding for the IsoDAR neutrino experiment. The shielding is asymmetric, having a larger thickness towards the KamLAND detector. The KamLAND detector with the surrounding buffer region and water layer is also shown.

radioactive decay give a less significant contribution to the total number of gammas. Low energy gammas are produced also in proton inelastic, deuteron inelastic, ion inelastic, alpha inelastic and photon nuclear processes, apart from the ones mentioned above (figure 24). The calculated gamma background is 2.38×10^{-24} gammas/POT with energies above 3 MeV and is produced in the detector mainly by inelastic interactions on carbon (2.31×10^{-24} gammas/POT) and at a smaller rate by neutron capture on hydrogen (5.69×10^{-26} gammas/POT) with a peak energy of 2.2 MeV. For 4 m of shielding towards the detector, the total numbers of gammas above 3 MeV is 2.7×10^{-24} gammas/POT. Therefore, for 7.88×10^{24} protons/5 years run, this corresponds to ≈ 22 gammas above 3 MeV for the 5 years experiment.

Figure 25 shows a vertical section through the current, latest version design of the target shielding for the IsoDAR neutrino experiment. The shielding is assymetric, having a larger thickness toward the KamLAND detector. The detector is also pictured here with the surrounding buffer region and the water layer.

8   Conclusion

A shielding system for the IsoDAR neutrino experiment was designed to meet the neutron flux irradiation requirements out of the shielding with a limiting value of $10^{-13} n/p/mm^2$. This value was obtained from neutron irradiation of the Kamioka rock samples and analysis of the radionuclides that were produced. New materials developed at Jefferson Laboratory like boron concrete together with layers of steel were used to design the shielding in the confined space of the current location

in the mine, without significant rock excavation. The radionuclides produced in the rock were identified and the ones that give a significant contribution to the total induced activation were the long lived isotopes like ^{60}Co, ^{22}Na, ^{152}Eu, and ^{154}Eu. A spatial distribution of the activity on the cavern wall identified the hot spots and the activity for these spots is below the required limitation of 0.1 Bq/g after 5 years run plus 2 years cool down period for a 2 m shielding. The neutron and gamma physics backgrounds in the KamLAND detector were simulated for the 5 years experiment and it was found that the levels at which they are produced do not give a significant background for detecting the IBD and ES physics signals.

Acknowledgments

References

[1] *KamLAND — Kamioka Liquid Scintillator Antineutrino Detector webpage*, http://www.awa.tohoku.ac.jp/kamlande.

[2] International Atomic Energy Agency, *Application of the concepts of exclusion, exemption and clearance*, IAEA safety standards series, RS-G-1.7, Radiation Safety Guide, Vienna, Austria (2004).

[3] M. Abs et al., *IsoDAR@KamLAND: a conceptual design report for the technical facility*, arXiv:1511.05130.

[4] IsoDAR collaboration, *IsoDAR@KamLAND: a conceptual design report for the conventional facilities*, arXiv:1710.09325.

[5] T.N.S.A. group, *Recommendations to the Department of Energy and the National Science Foundation on a future U.S. program in neutrino oscillations*, https://science.osti.gov/-/media/hep/pdf/files/pdfs/nusagfinalreportjuly13_2007.pdf.

[6] T.P. panel, *Report of the particle physics project prioritization panel*, https://science.osti.gov/-/media/fes/fesac/pdf/2019/201903/FESAC_AJL_Lankford.pdf.

[7] LSND collaboration, *Evidence for neutrino oscillations from the observation of $\bar{\nu}_e$ appearance in a $\bar{\nu}_\mu$ beam*, *Phys. Rev.* **D 64** (2001) 112007 [hep-ex/0104049].

[8] MiniBooNE collaboration, *Improved search for $\bar{\nu}_\mu \to \bar{\nu}_e$ oscillations in the MiniBooNE experiment*, *Phys. Rev. Lett.* **110** (2013) 161801 [arXiv:1303.2588].

[9] G. Mention et al., *The reactor antineutrino anomaly*, *Phys. Rev.* **D 83** (2011) 073006 [arXiv:1101.2755].

[10] J.M. Conrad and M.H. Shaevitz, *Multiple cyclotron method to search for CP-violation in the neutrino sector*, *Phys. Rev. Lett.* **104** (2010) 141802 [arXiv:0912.4079].

[11] J.M. Conrad, M.H. Shaevitz, I. Shimizu, J. Spitz, M. Toups and L. Winslow, *Precision $\bar{\nu}_e$-electron scattering measurements with IsoDAR to search for new physics*, *Phys. Rev.* **D 89** (2014) 072010 [arXiv:1307.5081].

[12] KamLAND collaboration, *Precision measurement of neutrino oscillation parameters with KamLAND*, *Phys. Rev. Lett.* **100** (2008) 221803 [arXiv:0801.4589].

[13] A. Bungau, J. Alonso, L. Bartoszek, J. Conrad, M. Shaevitz and J. Spitz, *Optimizing the ^8Li yield for the IsoDAR neutrino experiment*, 2019 *JINST* **14** P03001 [arXiv:1805.00410].

[14] M. Abs et al., *IsoDAR@KamLAND: a conceptual design report for the technical facility*, arXiv:1511.05130.

[15] Thomas Jefferson National Accelerator Facility, *New shielding is designed to put the block on neutrons*, https://www.jlab.org/news/stories/new-shielding-designed-put-block-neutrons.

[16] M.B. Chadwick et al., *ENDF/B-VII.1 nuclear data for science and technology: cross sections, covariances, fission product yields and decay data*, *Nucl. Data Sheets* **112** (2011) 2887.

[17] *TENDL*-2014*: TALYS-based evaluated nuclear data library*, https://www-nds.iaea.org/public/download-endf/TENDL-2014.

[18] *TALYS webpage*, https://tendl.web.psi.ch/tendl_2019/talys.html.

[19] T. Nakagawa et al., *Japanese evaluated nuclear data library version* 3 *revision-*2*: JENDL*-3.2, *J. Nucl. Sci. Technol.* **32** (1995) 1259.

[20] Y.N. Shubin et al., *Cross section data library MENDL-*2 *to study activation and transmutation of materials irradiated by nucleons of intermed. energies*, INDC(CCP)-385, International Atomic Energy Agency, Vienna, Austria (1995).

[21] J.P. Wellisch, *GEANT*4 *physics validation for large HEP detectors*, *Nucl. Instrum. Meth.* **A 502** (2003) 669.

[22] F.M. Waterman, F.T. Kuchnir, L.S. Skaggs, R.T. Kouzes and W.H. Moore, *Neutron spectra from* 35 *and* 46 *MeV protons,* 16 *and* 28 *MeV deuterons, and* 44 *MeV* ^{3}*He ions on thick beryllium*, *Med. Phys.* **6** (1979) 432.

[23] S.W. Johnsen, *Proton-beryllium neutron production at* 25–55 *MeV*, *Med. Phys.* **4** (1977) 255.

[24] H.I. Amols et al., *Physical characterization of neutron beams produced by protons and deuterons of various energies bombarding beryllium and lithium targets of several thicknesses*, *Med. Phys.* **4** (1977) 486.

[25] M.M. Meier et al., *Differential neutron production cross sections and neutron yields from stopping-length targets for* 113 *MeV protons*, *Nucl. Sci. Eng.* **102** (1989) 310.

[26] P.H. Heintz, S.W. Johnsen and N.F. Peek, *Neutron energy spectra and dose-distribution spectra of cyclotron-produced neutron beams*, *Med. Phys.* **4** (1977) 250.

[27] R. Madey, F.M. Waterman and A.R. Baldwin, *Neutron spectra at* 0° *from* 83.7 *MeV deuterons and* 100.2 *MeV protons on beryllium*, *Med. Phys.* **4** (1977) 322.

[28] G.H. Harrison, E.K. Balcer-Kubiczek and C.R. Cox, *Dosimetric properties of p*(90)+*(Be+Ta) and p*(101)+*(Be+Al) neutrons*, *Med. Phys.* **7** (1980) 348.

[29] M. Osipenko et al., *Measurement of neutron yield by* 62 *MeV proton beam on a thick beryllium target*, *Nucl. Instrum. Meth.* **A 723** (2013) 8 [arXiv:1302.7226].

[30] I. Tilquin et al., *Experimental measurements of neutron fluxes produced by proton beams (*23–80 *MeV) on Be and Pb targets*, *Nucl. Instrum. Meth.* **A 545** (2005) 339.

[31] *MCNPX webpage*, https://mcnpx.lanl.gov.

[32] KAMLAND collaboration, *Production of radioactive isotopes through cosmic muon spallation in KamLAND*, *Phys. Rev.* **C 81** (2010) 025807 [arXiv:0907.0066].

[33] A. Tang, G. Horton-Smith, V.A. Kudryavtsev and A. Tonazzo, *Muon simulations for Super-Kamiokande, KamLAND and CHOOZ*, *Phys. Rev.* **D 74** (2006) 053007 [hep-ph/0604078].

[34] L. Winslow, *First solar neutrinos from KamLAND: a measurement of the* ^{8}*B solar neutrino flux*, Ph.D. thesis, University of California, Berkley, CA, U.S.A. (2008).